Title

Quantum Yields, Surface Quenching, and Passivation Efficiency for Ultrasmall Core/Shell Upconverting Nanoparticles

Journal

Journal of the American Chemical Society, 140(14)

ISSN

0002-7863

Authors

Würth, Christian
Fischer, Stefan
Grauel, Bettina
et al.

Publication Date

2018-04-11

DOI

10.1021/jacs.8b01458

Peer reviewed

Quantum yields, surface quenching and passivation efficiency for ultra-small core/shell upconverting nanoparticles

Christian Würth[1], Stefan Fischer[2,3], Bettina Grauel[1], A. Paul Alivisatos[2,3,4,5] and Ute Resch-Genger[1*]

[1] Federal Institute for Materials Research and Testing (BAM), Richard-Willstätter-Straße 11, 12489 Berlin, Germany;

[2]Department of Chemistry, University of California—Berkeley, Berkeley, California 94720, USA

[3]Department of Materials Science and Engineering, University of California—Berkeley, Berkeley, California 94720, USA

[4]Materials Sciences Division, Lawrence Berkeley National Laboratory, Berkeley, California 94720, USA

[5]Kavli Energy NanoScience Institute, Berkeley, California 94720, USA

KEYWORDS Upconversion, nanoparticle, passivation, shell, quantum yields, quenching.

ABSTRACT: We synthesized and characterized a set of ultra-small hexagonal-phase $NaGdF_4$: 20% Yb^{3+}, 2% Er^{3+} upconversion nanoparticles with core diameters of 3.7 ± 0.5 nm. In order to assess passivation effects and the influence of possible core-shell intermixing, and identify optimum particle structures for combined imaging in the visible and near infrared (VIS-NIR; 410-850 nm) and short-wave infrared (SWIR;1520 nm), $NaYF_4$ shells of varying thicknesses (monolayer to 10 nm) were introduced and the influence of this parameter on the upconversion and downshifting photoluminescence of these particles was studied at different excitation power densities. This included excitation power-dependent emission spectra, slope factors, quantum yields, and exited state decay kinetics. These measurements revealed enhancement factors of the upconversion quantum yield of >10,000 in the low power region and an excitation power density-independent quantum yield of the downshifted emission at 1520 nm between 0.1 and 14%. The optimized shell thickness for combined VIS and SWIR imaging was identified to 5 nm. Moreover, lifetimes and quantum yields can be continuously tuned by shell thickness which can be exploited for lifetime multiplexing and encoding. The fact that, we did not observe a saturation of the upconversion quantum yield or the exited state decay kinetics with increasing shell thickness is ascribed to a strong intermixing of the active core with the inert shell during the shelling procedure. This underlines the potential of spectroscopic tools to detect cation intermixing.

Introduction Lanthanide (Ln^{3+}) ions have high potential as reporters and active materials for optical technologies and form already the core of key technologies in lighting applications like light emitting diodes (LEDs) and solid-state lasers. The 4f electron orbitals of lanthanides provide a manifold of energy levels enabling a multitude of optical transitions accounting for many sharp emission bands. As 4f–4f transitions of Ln^{3+} ions are parity and commonly also spin forbidden, these ions show long excited state lifetimes enabling multistep energy transfer processes between resonant energy levels of the same as well as different Ln^{3+} ions. This has been exploited for downconversion (quantum cutting) and upconversion of photons e.g., to improve the performance of solar cells.[1-3] Within a decade, Ln^{3+}-based upconversion nanoparticles (UCNPs) with their multi band emission in the visible (VIS) up to the short wavelength infrared (SWIR)[4,5] have evolved from objects of mere fundamental research to emerging tools for drug delivery[6,7], contrast agents for magnetic resonance tomography (MRI)[8-10], reporters for optical imaging[7,11], assays in complex media[11,12], lifetime multiplexing[13,14], and recently also SWIR imaging[4,5,15] as well as superresolution microscopy[16]. Sub 10-nm UCNPs of different chemical composition have been meanwhile used also for single particle imaging studies.[17-20]

The efficiency of non-linear optical processes like upconversion in nanocrystals is largely determined by surface effects. Size[21], doping concentration[19], surface modification with protecting shells[22], and spatial position and local separation of dopands[23] allow to tune upconversion through control of energy migration[24]. Particularly for small UCNPs with a large surface area-to-volume ratio, surface quenching rates are high and passivation is typically achieved with a non-active inert shell.[25-30] This shell heals surface defects and shield

optically active Ln^{3+} ions in the core from luminescence quenching molecules like surface ligands and solvent molecules with high energy vibrations, that can interact with the excited states of Er^{3+} and Yb^{3+} by dipole-dipole interactions.[25] The shell thickness required for effective passivation and shielding is also dependent on excitation power density (P) as upconversion is a nonlinear process. Hence, different shell thicknesses may be required to optimize UCNP performance for different applications, for example, as reporters in assays and under microscopic conditions or as donors in resonance energy transfer nanosensors.[31,32]

Here, we focus on the design of efficient core-shell UCNPs with sub 4 nm ß-$NaGdF_4$ cores co-doped with 20% Yb^{3+} and 2% Er^{3+} and stepwise growth of shell layers of ß-$NaYF_4$.[8,33] Passivation efficiencies are quantified based upon P-dependent upconversion and downshifted luminescence spectra, quantum yields, and excited state population dynamics with the overall goal to identify optimum nanostructures for dual band imaging in the VIS and SWIR.

Results and discussion

We synthesized ß-$NaGdF_4$ UCNPs co-doped with 20% Yb^{3+} and 2% Er^{3+} for upconversion of photons at around 980 nm to mostly green ($^2H_{9/2}$, $^4S_{3/2} \rightarrow {}^4I_{15/2}$) and red ($^4F_{9/2} \rightarrow {}^4I_{15/2}$) photons as shown in the energy level diagram in Figure 1c. For shell growth around the active core UCNPs, $NaYF_4$ precursors were added sequentially, the amount of which was calculated to provide passivation shells with thicknesses ranging from roughly one monolayer to 10 nm (see schematic and TEM images in Figure 1b used here for the calculation of the obtained shell thicknesses d_s assuming no core-shell intermixing given here as well as the Experimental Section and the SI for details). The drastic influence of the added shelling material on the upconversion luminescence of $NaGdF_4$: 20% Yb^{3+}, 2% Er^{3+} nanoparticles with a core diameter of 3.7 ± 0.5 nm is shown in Figures 1c and 1d). Our observations reveal fundamental differences in the relative spectral contributions of the visible and NIR emission bands to the overall upconversion luminescence between particles with the amount of shell material added to from thick and thin shells. With increasing d_s, the contribution of the green emission ($^2H_{9/2}$, $^4S_{3/2} \rightarrow {}^4I_{15/2}$) increases constantly from about 40% to 60% for d_S = 4.5 nm (Figure 1d and SI, Figure S2) driven by $^4S_{3/2}$, whereas the red emission ($^4F_{9/2} \rightarrow {}^4I_{15/2}$), accounting for about 15 % of the overall upconversion luminescence, is affected comparably little. This is also the case for the 850nm emission ($^4S_{3/2} \rightarrow {}^4I_{13/2}$), which remains almost constant for $d_S \geq 0.5$ nm with an increase of 5%. The 810nm emission ($^4I_{9/2} \rightarrow {}^4I_{15/2}$) is highest for thin shells with consequently higher surface quenching rates and steadily decreases with increasing amount of shell material. The $^4I_{9/2}$ level is populated via Er^{3+}-Er^{3+} energy transfer which involves the $^4I_{13/2}$-level or population via non-radiative deactivation of the $^4F_{9/2}$ level. Obviously, under these “quenched” conditions, the $Er^{3+} \rightarrow Er^{3+}$ energy transfer efficiency can compete with ETU populating the green emitting energy levels $^2H_{11/2,}$ and $^4S_{3/2}$.

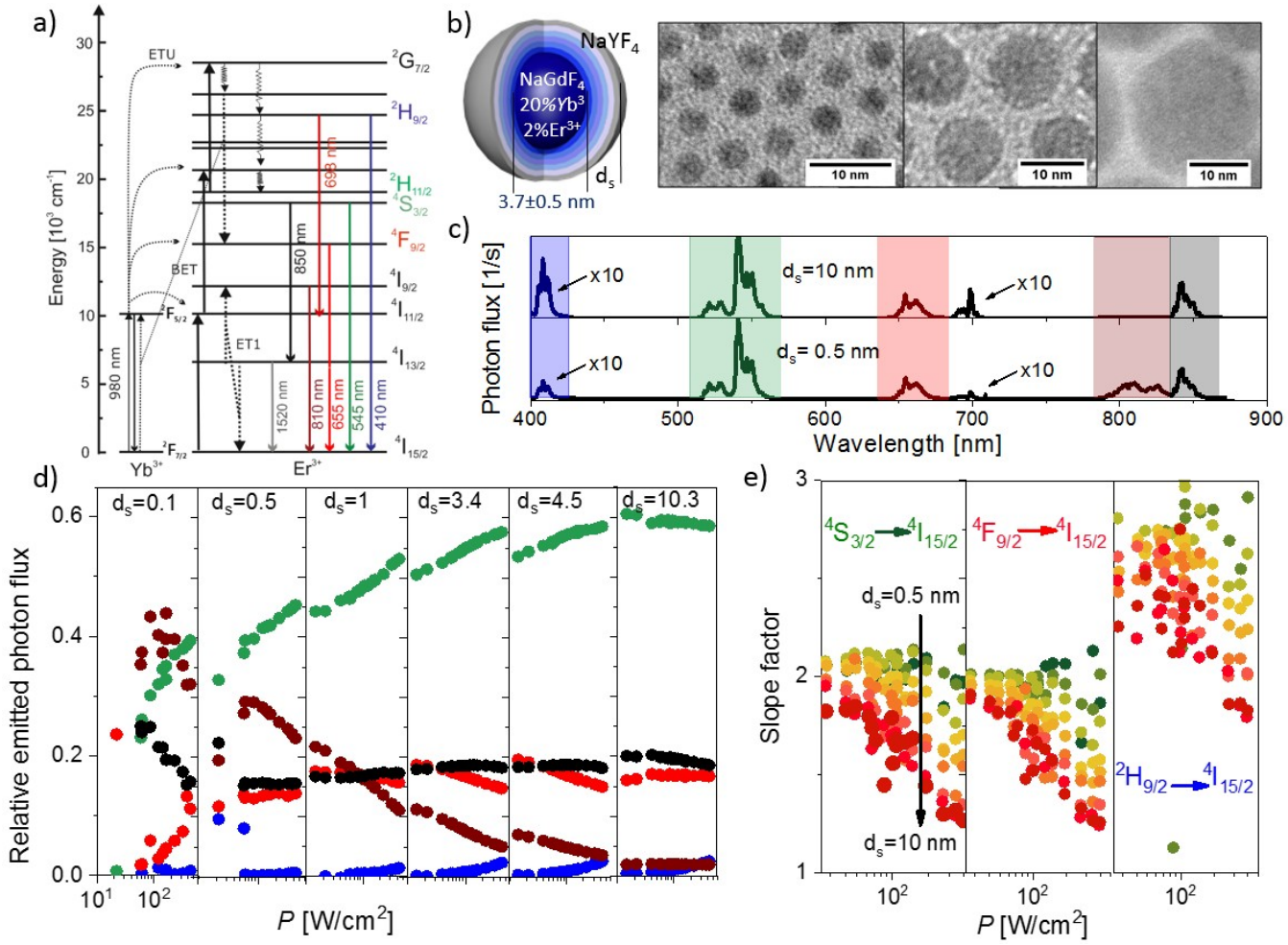

Figure 1: Power-dependent upconversion luminescence of hexagonal $NaGdF_4$: 20% Yb^{3+}, 2% Er^{3+} particles with a core diameter of 3.7 ± 0.5 nm dispersed in cyclohexane and passivated with a $NaYF_4$ shell of varying thickness (d_s): a) Energy level diagram of Yb^{3+}, Er^{3+} co-doped $NaYF_4$, ET: energy transfer, ETU: energy transfer upconversion, BET: back energy transfer, b) Schematic of the core shell particles and corresponding TEM images (see also SI), c) Emission spectra for two different shell thickness at a *P* of 20 W/cm², d) Relative emitted photon flux of the most important emission bands (given in the same color code as used in the energy level diagram), e) Power-dependent slope factors (*n*) for the $^2H_{11/2}$,$^4S_{3/2}$, $^4F_{9/2}$,$^2H_{9/2}$ -levels and different shell thicknesses (color code: thin shells in green to thick shells red).

The relative contributions of the different emission colors also depend on *P*. For shells up to d_s = 4.5 nm (particle diameter 12.4±1.1 nm), the green emission increases strongly with increasing *P* (Figure 1d and SI, Figure S2). This is also the case for the blue emission. The contribution of the 810 nm emission decreases with increasing *P*. The 655 nm and 850 nm emission are less affected by *P* for $d_s \geq 0.5$ nm. For $d_s > 4.5$ nm, the spectral distribution of the upconversion luminescence changes only slightly with *P*. When adding enough shell material to form 10 nm thick shells, the green-to-red ratio is independent of *P*. This is a rather astonishing finding and suggests that there is intermixing of the core and the shell and accordingly, depletion of the doping concentration in the alloyed volume.

The slope factors (n, / P^n) were calculated from the *P*-dependence of the emitted photon flux (see Figure 1e)). For low *P* when the decay rates are much lower than the ETU rates, *n* represents the number of photons involved in the upconversion process. A decreasing value of *n*(*P*) indicates an increasing ETU rate approaching the decay rate of the corresponding level.[34,35] For UCNPs with small amount of shell material i.e. thin shells, we calculated *n* of around 2 for the green and also the red emission band at low *P*, indicating biphotonic transitions. This contradicts common reports on the red emission becoming three photonic with increasing *P* which is accompanied by a strong increase in its relative contribution to the overall emission.[36,37] The *P*-independent emission contribution of the red $^4F_{9/2}$-level of our ultra-small UCNPs for $d_s > 0.5$ nm and the small slope factor indicate solely population by non-

radiative deactivation of the green and $^4I_{13/2}$, this population pathway is independent of P and d_s. For the blue emission, n is roughly 3. With increasing amount of shell material, the ETU rates for $^2H_{11/2}$, $^4S_{3/2}$, and $^4F_{9/2}$-levels approach the decay rates with increasing P as revealed by decreasing n and reach values of 1.25 for the red and green and 1.8 for the blue emission band, respectively.

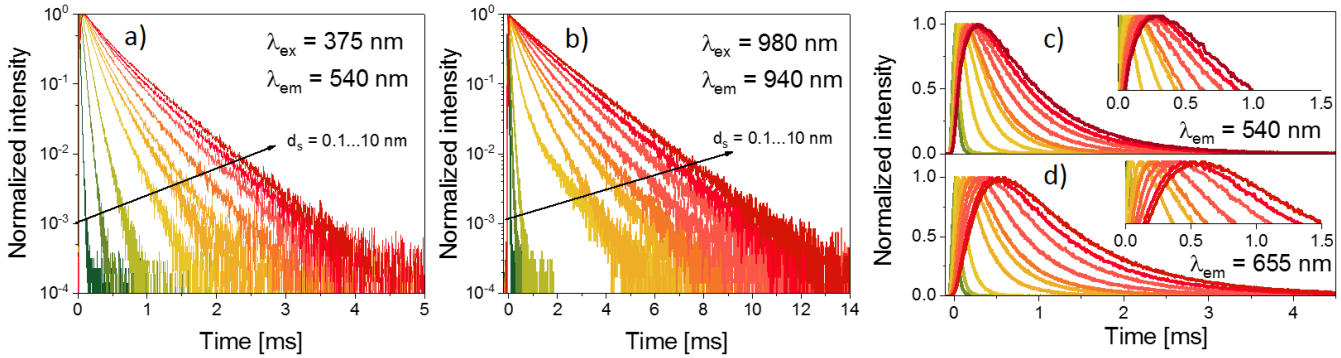

Figure 2: Decay curves of UCNPs dispersed in cyclohexane with d_s varied from 0.1 to 10 nm. a) green Er^{3+} emission under 375 nm excitation (545 nm - downshifting); b) Yb^{3+} emission with 980 nm excitation (940 nm - downshifting); c) and d) green and red upconversion emission under 980 nm excitation.

The complex decay kinetics of coupled multi ionic systems like upconversion materials present elegant tools to assess surface passivation effects and the efficiency of shielding optically active Ln^{3+} ions, which reduces non-radiative rates. The decay curves of the Er^{3+} and the Yb^{3+} emission bands of our $NaGdF_4$: 20% Yb^{3+}, 2% Er^{3+} core-shell UCNPs dispersed in cyclohexane are shown in Figure 2. The lifetimes were determined for direct excitation at 375 nm (Figure 2a; detection at 540 nm), 980 nm (Figure 2b; detection at 940 nm), and 980 nm excitation using ETU (Figure 2c, d). For all excitation pathways, the luminescence decays of the excited Er^{3+} and Yb^{3+} energy levels show longer lifetimes with increasing amount of shell material and increasing d_s calculated from the TEM images. This reveals the constant reduction of the respective non-radiative decay rates by surface passivation and Ln^{3+} shielding. In all cases, the lifetime prolongation depends linear on the amount of shell material added (see Figure 3), which agrees well with reports from other groups.[38,39] Nevertheless, for the shell thicknesses studied here, the lifetimes do not reach a constant maximum value, which should be close to the intrinsic lifetime of the ion's energy level. This becomes obvious when comparing the values for the $^4F_{9/2}$ (655 nm) and $^4S_{3/2}$ (545 nm) Er^{3+} energy levels resulting for excitation via ETU (980 nm, $Yb^{3+} \longrightarrow Er^{3+}$) and direct Er^{3+} excitation (at 375 nm), respectively (see Figure S5). ETU excitation leads to a more pronounced increase in the decay and rise time of the red compared to the green level (see Figure 2c and 3 (left)) and thus, its decay rate seems to be smaller. For direct Er^{3+} excitation, the lifetimes of the green and red emission are shorter and match closely. The longer rise time points to a two photonic population channel for the red via $^4S_{3/2}$ or even ETU from $^4I_{13/2}$.

The decay kinetics of directly excited Er^{3+} are used to estimate the radiative decay rates. In this case, ET processes can occur as well. The dependence of the decay time vs d_s for the Yb^{3+} emission as well as the corresponding decay rates are shown in Figure 3a. The lifetime of Yb^{3+} increases with a slope of $\frac{\partial \tau_{Yb}}{\partial d_s} \approx 148[\mu s/nm]$ and that of the green and red Er^{3+} levels with a slope of $\frac{\partial \tau_{Er}}{\partial d_s} \approx 48[\mu s/nm]$ (see also SI). From these fits, we estimated the trend of the decay rates which is determined by non-radiative processes, e.g. surface quenching (see Figure 3b). For the bare UCNP core, we obtained a decay rate of $4 \cdot 10^4$ 1/s for both Er^{3+} levels. This value is reduced by a factor of about 4 already with a very thin shell in the range of one monolayer. With d_s of around 4.5 nm, the rate is further diminished to roughly $5 \cdot 10^3$ 1/s and reaches $2 \cdot 10^3$ 1/s for d_s of around 10 nm. For Yb^{3+}, the passivation is even more effective reducing the decay rate of bare core UCNPs of $1.3 \cdot 10^5$ 1/s to $1.4 \cdot 10^4$ 1/s (by a factor of 9) for particles with a monolayer shell, to $1.5 \cdot 10^3$ 1/s (by a factor of 87) for a 4.5 nm shell, and to $6.5 \cdot 10^2$ 1/s (by a factor of 200) for a 10 nm shell, respectively. The Yb^{3+} lifetime of 1500 µs for a UCNP with 10 nm shells is close to that of the bulk material (ca. 2000 µs)[36]. The passivation efficiency of the shell can be underpinned by a comparison with the Yb^{3+} lifetime of about 120 µs of 23 nm-sized core-only β-$NaYF_4$: Yb Er UCNPs (same surface ligand oleic acid, dispersed in cyclohexane; assuming that matrix induced changes between β-$NaYF_4$ and β-$NaGdF_4$ are small[40]).[36]

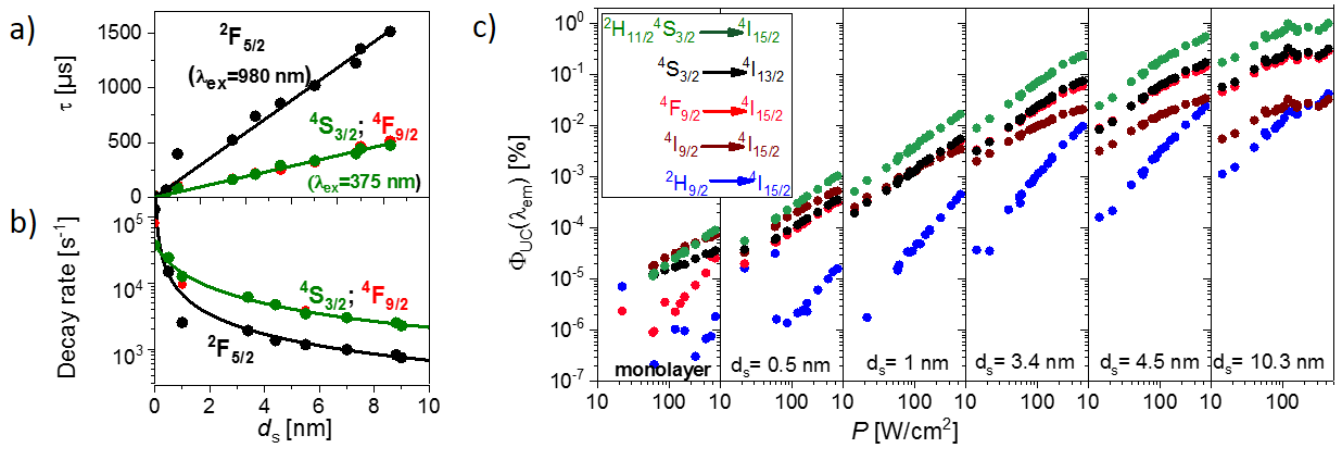

Figure 3: a) Fitted intensity-weighted decay times of the downshifted emission (solid circles) of Yb^{3+} (black) and Er^{3+} (green; red); b) Estimated decay rates of the downshifted emission (solid circles) of Yb^{3+} (black) and Er^{3+} (green; red); c) *P*-dependence of the upconversion quantum yields (Φ_{UC}) of the different emission bands.

The large non-radiative rates and the effective passivation of Yb^{3+} are also reflected by the *P*-dependent Φ_{UC} values of the different emission bands ($\Phi_{UC}(\lambda_{em})$) < 900 nm shown in Figure 3c. With increasing d_s, particularly the efficiency of the biphotonic green emission steadily increases by 4 orders of magnitude from one monolayer to a 10 nm shell. The green emission is the strongest one for d_s > 0.5 nm (Figure 1 and 3c), with its Φ_{UC} reaching 1% for high *P* of >100 W/cm^2 and d_s = 10 nm. Φ_{UC} of the red and blue emission amount only to 0.3 % and 0.04 %, respectively. This behavior is in contrast to that observed by us for 23 nm-sized core-only β-$NaYF_4$: Yb,Er UCNPs. In this case, the red emission was the strongest one for high *P* and the green luminescence was dominant in the lower *P* region (here <100 W/cm^2).[36,37] For these 23 nm-sized core-only β-$NaYF_4$: Yb,Er UCNPs, the $^4F_{9/2}$-level is mainly populated by non-radiative relaxation of $^4S_{3/2}$ (two photonic process) in the low *P*-region and by three photonic processes involving higher energy levels in the high *P*-range. This comparison (see also Figure 1e, red Er^{3+} emission, middle panel) underpins that not only the excited state lifetime, but also the number of active Ln^{3+} ions as well as their spatial arrangement are important for both population and depopulation pathways. On average, our ultra-small β-$NaGdF_4$: Yb, Er core-shell UCNPs contain only 73 Yb^{3+} sensitizer ions and 7 Er^{3+} activator ions. At *P* of ~400 W/cm^2, only approximately 2.5 Yb^{3+} ions per particle are excited per millisecond. From this rough estimation, the Yb^{3+} decay rate equals the excitation rate for a for d_s≈ 3-4 nm (Figures 3 a) and 3 b). For thinner shells, the decay rates are in the same order of magnitude. For d_s < 1 nm, the decay rates strongly exceed the Yb^{3+}excitation rate and consequently, the probability for energy transfer dramatically decreases. This is also reflected by the slope factors. The small number of sensitizer ions per particle in combination with the fast decay rates of Yb^{3+} and Er^{3+} in the order of 10^3 1/s leads to a low probability for energy migration from an excited sensitizer to an "excited" activator, i.e., an activator with an already populated $^4S_{3/2}$-level.

Three photonic processes can be expected for sufficient passivated particles with lifetimes near the ones of bulk material. The back-energy transfer (BET process) via cross relaxation (shown in Figure 1 in the energy level diagram) is required for the three-photonic population of the red emitting $^4F_{9/2}$ level. We expect the rate for this process to be strongly diminished compared to bigger core only particles. This can also be seen in the *P*-dependent decrease in the ratio of the red and blue emitted photon fluxes (see Figure S6) All these observations in combination with the decay kinetics point to an increasing ion distance reducing the energy transfer probability which would consequently suggest a doping depletion of the active core and therefore an intermixing of the core and shell material.

The overall Φ_{UC} values of our ultra-small $NaGdF_4$: Yb, Er UCNPs range from 0.00004% for the bare to 1.7% for the thickest-shelled particles for *P* of around 420 W/cm^2. As follows from Figure 4, a very thin shell of roughly one monolayer accounts already for a Φ_{UC} increase by a factor of 5 for the highest *P* used here and allows the determination of Φ_{UC} even at low *P* of roughly 20 W/cm^2. For the highest *P* of 420 W/cm^2, the UC luminescence is enhanced by a factor of 42,500 for a 10nm shell compared to bare nanoparticles. For lower *P* the enhancement is even higher (see Figure S7). For d_s < 1 nm, Φ_{UC} increases exponentially and for d_s > 1 nm, the enhancement rises linearly with a slope of ca. $\frac{\partial \Phi_{UC}}{\partial d_s} \approx 0.2\,[nm^{-1}]$.

Assuming dipole-dipole energy transfer interactions between the sensitizer ions and surface ligands as non-radiative deactivation channel of the excited energy levels of the Ln^{3+} ions, a distance of ~10 nm between the emissive ions and the ligands should prevent surface quenching rates proportional to d_s^{-4}.[41,42] The similar linear increase of Φ_{UC} and decay times (Figures 3 and 4) observed for our core-shell UCNPs suggests incorporation of optically active Ln^{3+}ions into the shell and/or direct intermixing of core and shell material during the synthesis of the core-shell UCNPs.[43,44] Possible explanations are the partly dissolution of the outer core layer during the reaction's heating phase with continuous incorporation of the dissolved core ions during the shell growth and/or competing Oswald-Ripening of similar sized nanoparticles made of the core and shell material. The resulting doping gradient in the shell is particularly critical for ultra-small nanoparticles that contain only a small number of active Ln^{3+} ions per particle. A reduction of the overall density of emissive Ln^{3+} ions per particle leads to much more pronounced luminescence effects compared to larger UCNPs. This underlines the importance of a precise control of the core-shell interface for the design of complex and multifunctional nanoprobes, especially for very small nanoparticles desired for bioimaging. Complete core passivation can be most likely achieved by reducing the intermixing of core and shell material during the shelling procedure by successive purification of the reaction solutions after each shelling step and by layer-by-layer epitaxial growth of the shell. [23,45,46] However, all reported shelling techniques seem to result in intermixing of the core and shell material. This highlights the need for better shelling procedures as well as characterization techniques to study the core/shell interface in more detail. The recent work from Hudry et al.[44] and Xue et al.[47] are steps into the right direction in precisely characterizing the core/shell intermixing.

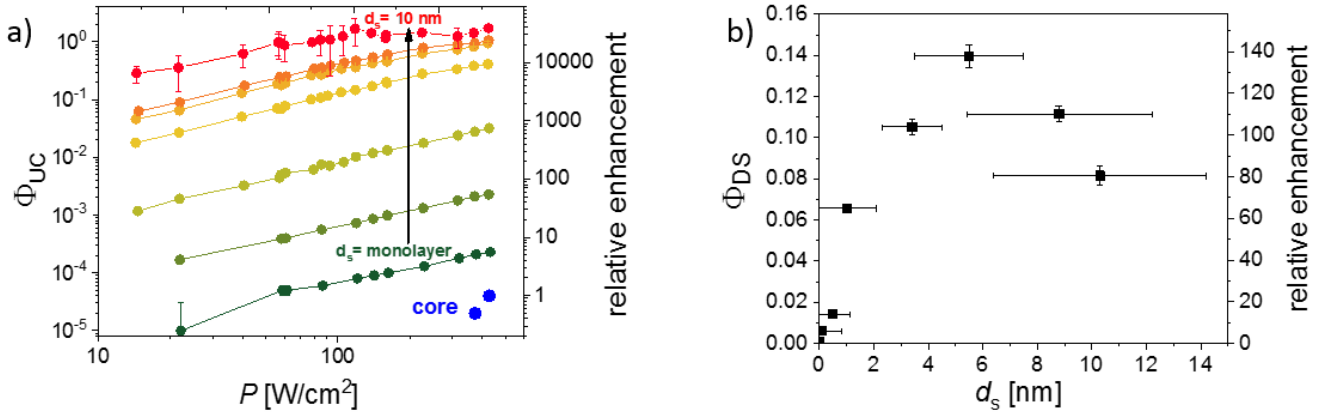

Figure 4: a) *P*-dependent Φ_{UC} of the ultra-small β-$NaGdF_4$: Yb Er UCNPs cores (blue) dispersed in cyclohexane with shell thickness varying between one monolayer and 10 nm (lines are a guide to the eye only); the larger uncertainties given for UCNPs with thick shells are caused by low absorbances of the sample due to the small particle concentrations. b) Shell thickness-dependence of Φ_{DS} for the β-$NaGdF_4$: Yb Er UCNP series averaged over all *P* values (the error bars indicate the uncertainty for the shell thickness determination from TEM measurements).

The quantum yield of the downshifted emission (Φ_{DS}) of Er^{3+} at 1520 nm is independent of *P* as commonly observed for a Stokes shifted luminescence. Φ_{DS} increases with increasing d_s and reaches a maximum value of 14 % for d_s of 5 nm. This equals an enhancement factor of around 140 compared to bare particles. For thicker shells, Φ_{DS} decreases again. This trend displays the strong quenching of Yb^{3+} for d_s <5 nm, which is also reflected by the strongly changing spectral contributions to Φ_{UC} (Figure 3). The decrease of Φ_{DS} for shells with d_s > 5 nm is attributed to the hampering of non-radiative deactivation of $^4I_{11/2}$ and population of $^4I_{13/2}$ by the passivating shell. Similar effects have been also reported for β-$NaYF_4$: 33% Yb^{3+}, 5% Er^{3+} UCNPs with core sizes of 23.8 ± 1.2 nm and β-$NaLuF_4$ shells between 0.3 to 13.0 nm.[25]

The quantum yields of the upconverted and downshifted emission of our ultra-small hexagonal-phase $NaGdF_4$: 20% Yb^{3+}, 2% Er^{3+} UCNPs reveal that the optimum shell thickness for combined VIS and SWIR imaging for ultra-small particles is around 5 nm.

Conclusion and Outlook

We synthesized ultra-small hexagonal $NaGdF_4$: 20% Yb^{3+}, 2% Er^{3+} upconversion nanoparticles (UCNPs) with a core size of 3.7 ± 0.5 nm and used a typical shelling procedure to passivated the surface of these particles with differently thick inactive β-$NaYF_4$ shells. These particles were systematically characterized to quantify the

influence of the shell thickness on the population dynamics of the Yb^{3+} and Er^{3+} energy levels involved in energy transfer upconversion (ETU) and upconversion luminescence to identify optimum particle architectures for combined imaging in the visible (VIS) and shortwave infrared (SWIR). Our results indicate a core shell intermixing during the shelling procedure. Measurements of the upconversion quantum yield (Φ_{UC}) and the quantum yield of the downshifted Er^{3+} emission (Φ_{DS}) around 1520 nm revealed that the added amount of shel precursor material to form a shell with a thickness of around 5 nm (particle diameter <15 nm) represents the best compromise between efficient upconversion with Φ_{UC} of roughly 1% at 420 W/cm^2 and bright SWIR emission with Φ_{DS} up to 14%, independent of *P*. For the thickest shell of 10 nm, Φ_{UC} reaches 1.7%, equaling an enhancement factor of 43,000 compared to bare particles. These data provide a quantitative measure for the influence of the passivation shell on upconversion photoluminescence at *P* values covering bioimaging and assay applications as well as spectroscopic studies.[32]

Our studies underline also the potential for emission color tuning as revealed by the dominating 810 nm emission for strongly quenched UCNPs with thin shells and the green emission becoming most pronounced for $d_s > 0.5$ nm. Moreover, the small size of our UCNPs favors a biphotonic population mechanism of the red $^4F_{9/2}$ level independent of *P* and d_s. This suggests that a critical number and density of active Ln^{3+} ions per particle is required for efficient three photonic population of the $^4F_{9/2}$ level. Our synthesis procedure allows also to tune the excited state lifetimes of the different emission bands by continuously adding shell precursors. This could be exploited for lifetime multiplexing and encoding.[48,49]

In the future, the continuously improving spectroscopic capabilities in the SWIR with less parasitic absorption and autofluorescence as well as strongly reduced scattering from tissue and blood components are expected to trigger the need for reporters with bright emission in this third optical window of bioimaging. UCNPs like our ultra-small core-shell systems are interesting candidates for such applications as well as for theranostics and medical diagnostics. There is nevertheless still room for improvement of their optical properties by rational and application-adapted design of particle architecture such as sharp core shell interfaces. This also includes boosting of brightness by enhancing the absorption cross section and the introduction of multifunctionality by co-doping with Gd^{3+} or a thin $NaGdF_4$ layer deposited on top of the inert passivation shell for magnetic resonance imaging (MRI), and exchanging the $NaYF_4$ shell for a $NaLuF_4$ shell for improved signals in computer tomography CT.

Experimental

Materials: The ß-$NaGdF_4$: 20% Yb^{3+} and 2% Er^{3+} core nanocrystals have been synthesized as reported in literature[8] with some modifications which are outlined in Fischer et al.[50]. In short, the molar ratios for the desired doping with the rare-earth acetate precursors were added into a three-necked-flask. Here, we used a total amount of 4 mmol in a 250 mL 3-neck flask and added 22 mL oleic acid and 68 mL 1-octadecene. The rare-earth acetates were dissolved under vacuum at 120 °C using a Schlenk line until a clear solution was obtained. Next, 10 mmol of sodium oleate and 16 mmol of ammonium fluoride were added at room temperature. This mixture was heated to 120 °C and switched between vacuum and argon atmosphere. After complete dissolution, the solution was heated to 270 °C under argon flow with a heating rate of 20 °C/min and kept at 270 °C for 45 min. The solution was then cooled down quickly (pressured air flow on outside of the flask).

Yttrium trifluoroacetate and sodium trifluoroacetate precursor solutions were used for the sequential shelling method as described in Fischer et al.[50] with some modifications. An amount of 2 mmol of the core sample was transferred into a 250 mL 4-neck flask to obtain 10 core-shell samples from the same core with different shell thicknesses (see SI). 10 mL oleylamine were added at room temperature and the mixture was degassed at 120 °C before heating to 300 °C under argon flow. The calculated amount of shell precursors was injected and samples were taken from the hot solution with a glass syringe using heat resistant gloves. Details on the shelling technique can be found in Fischer et al.[50]. The nanoparticles were washed twice with ethanol, centrifuges (3,000g for 5 min) and finally dispersed in cyclohexane.

Photoluminescence (PL) quantum yield Φ_{PL}: The quantum yield of the upconversion emission (Φ_{UC}), defined as the ratio of the number of emitted photons N_{em} with a wavelength $\lambda_{em} < \lambda_{abs}$, obtained from integral emission intensities of all UC emission bands (except for the sensitizer luminescence), and the number of absorbed photons N_{abs}, was determined absolutely with a previously described integrating sphere setup.[36,51] For the determination of the quantum yield of the long wavelength (downshifted, DS) emission of Er^{3+} at 1520 nm (Φ_{DS}), excited via energy transfer from Yb^{3+} to Er^{3+} the setup was equipped also with an Andor InGaAs-CCD array.[52]

Lifetime τ: lifetime measurements were performed with a commercially available Edinburgh Instruments setup (FLS980) with multi-channel scaling (MCS) equipped with a 980 nm (8W) laser diode for measurements of the upconversion luminescence (ETU from Yb^{3+} to Er^{3+}) and the downshifted emission of Yb^{3+} and with a 375nm pulsed light emitting diode of the

EPLED series for direct excitation of the downshifted Er^{3+} emission. A F-G03 R2658P photomultiplier in a cooled housing and a F-G05-02 high speed photomultiplier in a cooled housing with extended spectral range were used for signal detection.

TEM and XRD: TEM images were taken on a FEI Tecnai T20 equipped with a Gatan SC200 CCD camera and a LaB6 filament operated at 200 kV. XRD patterns were obtained using a Bruker D-8 GADDS diffractometer equipped with a Co Kα.

ASSOCIATED CONTENT

Supporting Information:. Synthesis, XRD, TEM decay curves, red green ratios "This material is available free of charge via the Internet at http://pubs.acs.org."

AUTHOR INFORMATION

Corresponding Author

* Ute Resch-Genger, E-mail: ute.resch@bam.de

Author Contributions

The manuscript was written through contributions of all authors. / All authors have given approval to the final version of the manuscript.

Funding Sources

DFG: agreement FI 2042/1-1; grant RE1203/18-1; COST Action CM1403

ACKNOWLEDGMENT

S.F. gratefully acknowledges the scholarship support from the German Research Foundation (DFG, agreement FI 2042/1-1). URG acknowledges financial support from the German Research Council (DFG; grant RE1203/18-1). Also, the European Upconversion Network (COST Action CM1403) is gratefully acknowledged.

REFERENCES

(1) Huang, X. Y.; Han, S. Y.; Huang, W.; Liu, X. G. *Chemical Society Reviews* **2013**, *42*, 173.

(2) de la Mora, M. B.; Amelines-Sarria, O.; Monroy, B. M.; Hernandez-Perez, C. D.; Lugo, J. E. *Solar Energy Materials and Solar Cells* **2017**, *165*, 59.

(3) Goldschmidt, J. C.; Fischer, S. *Advanced Optical Materials* **2015**, *3*, 510.

(4) Naczynski, D. J.; Tan, M. C.; Zevon, M.; Wall, B.; Kohl, J.; Kulesa, A.; Chen, S.; Roth, C. M.; Riman, R. E.; Moghe, P. V. *Nature Communications* **2013**, *4*.

(5) Tao, Z. M.; Dang, X. N.; Huang, X.; Muzumdar, M. D.; Xu, E. S.; Bardhan, N. M.; Song, H. Q.; Qi, R. G.; Yu, Y. J.; Li, T.; Wei, W.; Wyckoff, J.; Birrer, M. J.; Belcher, A. M.; Ghoroghchian, P. P. *Biomaterials* **2017**, *134*, 202.

(6) Yang, D. M.; Ma, P. A.; Hou, Z. Y.; Cheng, Z. Y.; Li, C. X.; Lin, J. *Chemical Society Reviews* **2015**, *44*, 1416.

(7) Shen, J.; Zhao, L.; Han, G. *Adv. Drug Deliv. Rev.* **2013**, *65*, 744.

(8) Johnson, N. J. J.; Oakden, W.; Stanisz, G. J.; Prosser, R. S.; van Veggel, F. *Chemistry of Materials* **2011**, *23*, 3714.

(9) Zhang, Y.; Wei, W.; Das, G. K.; Tan, T. T. Y. *Journal of Photochemistry and Photobiology C-Photochemistry Reviews* **2014**, *20*, 71.

(10) Liu, Q.; Feng, W.; Li, F. Y. *Coordination Chemistry Reviews* **2014**, *273*, 100.

(11) DaCosta, M. V.; Doughan, S.; Han, Y.; Krull, U. J. *Analytica Chimica Acta* **2014**, *832*, 1.

(12) Arppe, R.; Mattsson, L.; Korpi, K.; Blom, S.; Wang, Q.; Riuttamaki, T.; Soukka, T. *Analytical Chemistry* **2015**, *87*, 1782.

(13) Lu, Y. Q.; Zhao, J. B.; Zhang, R.; Liu, Y. J.; Liu, D. M.; Goldys, E. M.; Yang, X. S.; Xi, P.; Sunna, A.; Lu, J.; Shi, Y.; Leif, R. C.; Huo, Y. J.; Shen, J.; Piper, J. A.; Robinson, J. P.; Jin, D. Y. *Nature Photonics* **2014**, *8*, 33.

(14) Hoffmann, K.; Behnke, T.; Grabolle, M.; Resch-Genger, U. *Analytical and Bioanalytical Chemistry* **2014**, *406*, 3315.

(15) Kim, D.; Lee, N.; Park, Y. I.; Hyeon, T. *Bioconjugate Chemistry* **2017**, *28*, 115.

(16) Liu, Y. J.; Lu, Y. Q.; Yang, X. S.; Zheng, X. L.; Wen, S. H.; Wang, F.; Vidal, X.; Zhao, J. B.; Liu, D. M.; Zhou, Z. G.; Ma, C. S.; Zhou, J. J.; Piper, J. A.; Xi, P.; Jin, D. Y. *Nature* **2017**, *543*, 229.

(17) Gargas, D. J.; Chan, E. M.; Ostrowski, A. D.; Aloni, S.; Altoe, M. V. P.; Barnard, E. S.; Sanii, B.; Urban, J. J.; Milliron, D. J.; Cohen, B. E.; Schuck, P. J. *Nature Nanotechnology* **2014**, *9*, 300.

(18) Liu, Q.; Sun, Y.; Yang, T. S.; Feng, W.; Li, C. G.; Li, F. Y. *Journal of the American Chemical Society* **2011**, *133*, 17122.

(19) Chen, G. Y.; Ohulchanskyy, T. Y.; Kumar, R.; Agren, H.; Prasad, P. N. *Acs Nano* **2010**, *4*, 3163.

(20) Zheng, W.; Zhou, S. Y.; Chen, Z.; Hu, P.; Liu, Y. S.; Tu, D. T.; Zhu, H. M.; Li, R. F.; Huang, M. D.; Chen, X. Y. *Angewandte Chemie-International Edition* **2013**, *52*, 6671.

(21) Xue, X. J.; Uechi, S.; Tiwari, R. N.; Duan, Z. C.; Liao, M. S.; Yoshimura, M.; Suzuki, T.; Ohishi, Y. *Optical Materials Express* **2013**, *3*.

(22) Johnson, N. J. J.; Korinek, A.; Dong, C. H.; van Veggel, F. *Journal of the American Chemical Society* **2012**, *134*, 11068.

(23) Li, X. M.; Shen, D. K.; Yang, J. P.; Yao, C.; Che, R. C.; Zhang, F.; Zhao, D. Y. *Chemistry of Materials* **2013**, *25*, 106.
(24) Wang, F.; Deng, R. R.; Wang, J.; Wang, Q. X.; Han, Y.; Zhu, H. M.; Chen, X. Y.; Liu, X. G. *Nature Materials* **2011**, *10*, 968.
(25) Fischer, S.; Bronstein, N. D.; Swabeck, J. K.; Chan, E. M.; Alivisatos, A. P. *Nano Letters* **2016**, *16*, 7241.
(26) Rinkel, T.; Raj, A. N.; Duhnen, S.; Haase, M. *Angewandte Chemie-International Edition* **2016**, *55*, 1164.
(27) Wang, F.; Deng, R.; Liu, X. *Nat. Protocols* **2014**, *9*, 1634.
(28) Xie, X. J.; Gao, N. Y.; Deng, R. R.; Sun, Q.; Xu, Q. H.; Liu, X. G. *Journal of the American Chemical Society* **2013**, *135*, 12608.
(29) Zhang, F.; Che, R.; Li, X.; Yao, C.; Yang, J.; Shen, D.; Hu, P.; Li, W.; Zhao, D. *Nano Letters* **2012**, *12*, 2852.
(30) Vetrone, F.; Naccache, R.; Mahalingam, V.; Morgan, C. G.; Capobianco, J. A. *Advanced Functional Materials* **2009**, *19*, 2924.
(31) Muhr, V.; Würth, C.; Kraft, M.; Buchner, M.; Baeumner, A. J.; Resch-Genger, U.; Hirsch, T. *Analytical Chemistry* **2017**, *89*, 4868.
(32) Resch-Genger, U.; Gorris, H. H. *Analytical and Bioanalytical Chemistry* **2017**, *409*, 5855.
(33) Kobayashi, H.; Ogawa, M.; Alford, R.; Choyke, P. L.; Urano, Y. *Chem Rev* **2010**, *110*, 2620.
(34) Pollnau, M.; Gamelin, D. R.; Luthi, S. R.; Gudel, H. U.; Hehlen, M. P. *Physical Review B* **2000**, *61*, 3337.
(35) Liu, H. C.; Xu, C. T.; Lindgren, D.; Xie, H. Y.; Thomas, D.; Gundlach, C.; Andersson-Engels, S. *Nanoscale* **2013**, *5*, 4770.
(36) Kaiser, M.; Würth, C.; Kraft, M.; Hyppanen, I.; Soukka, T.; Resch-Genger, U. *Nanoscale* **2017**.
(37) Würth, C.; Kaiser, M.; Wilhelm, S.; Grauel, B.; Hirsch, T.; Resch-Genger, U. *Nanoscale* **2017**, *9*, 4283.
(38) Chen, D. Q.; Huang, P. *Dalton Transactions* **2014**, *43*, 11299.
(39) Wang, Y.; Smolarek, S.; Kong, X. G.; Buma, W. J.; Brouwer, A. M.; Zhang, H. *Journal of Nanoscience and Nanotechnology* **2010**, *10*, 7149.
(40) Wisser, M. D.; Fischer, S.; Maurer, P. C.; Bronstein, N. D.; Chu, S.; Alivisatos, A. P.; Salleo, A.; Dionne, J. A. *ACS Photonics* **2016**, *3*, 1523.
(41) Hossan, M. Y.; Hor, A.; Luu, Q.; Smith, S. J.; May, P. S.; Berry, M. T. *Journal of Physical Chemistry C* **2017**, *121*, 16592.
(42) Fischer, S.; Johnson, N. J. J.; Pichaandi, J.; Goldschmidt, J. C.; van Veggel, F. C. J. M. *Journal of Applied Physics* **2015**, *118*, 193105.
(43) Dühnen, S.; Haase, M. *Chemistry of Materials* **2015**, *27*, 8375.
(44) Hudry, D.; Busko, D.; Popescu, R.; Gerthsen, D.; Abeykoon, A. M. M.; Kübel, C.; Bergfeldt, T.; Richards, B. S. *Chemistry of Materials* **2017**, *29*, 9238.
(45) Li, X. M.; Wang, R.; Zhang, F.; Zhao, D. Y. *Nano Letters* **2014**, *14*, 3634.
(46) Hudry, D.; Busko, D.; Popescu, R.; Gerthsen, D.; Abeykoon, A. M. M.; Kubel, C.; Bergfeldt, T.; Richards, B. S. *Chemistry of Materials* **2017**, *29*, 9238.
(47) Xu, X.; Clarke, C.; Ma, C.; Casillas, G.; Das, M.; Guan, M.; Liu, D.; Wang, L.; Tadich, A.; Du, Y.; Ton-That, C.; Jin, D. *Nanoscale* **2017**, *9*, 7719.
(48) Grabolle, M.; Kapusta, P.; Nann, T.; Shu, X.; Ziegler, J.; Resch-Genger, U. *Analytical Chemistry* **2009**, *81*, 7807.
(49) Hoffmann, K.; Behnke, T.; Drescher, D.; Kneipp, J.; Resch-Genger, U. *ACS Nano* **2013**, *7*, 6674.
(50) Fischer, S.; Swabeck, J. K.; Alivisatos, A. P. *Journal of the American Chemical Society* **2017**, *139*, 12325.
(51) Würth, C.; Pauli, J.; Lochmann, C.; Spieles, M.; Resch-Genger, U. *Analytical Chemistry* **2012**, *84*, 1345.
(52) Hatami, S.; Würth, C.; Kaiser, M.; Leubner, S.; Gabriel, S.; Bahrig, L.; Lesnyak, V.; Pauli, J.; Gaponik, N.; Eychmuller, A.; Resch-Genger, U. *Nanoscale* **2015**, *7*, 133.

TOC 1

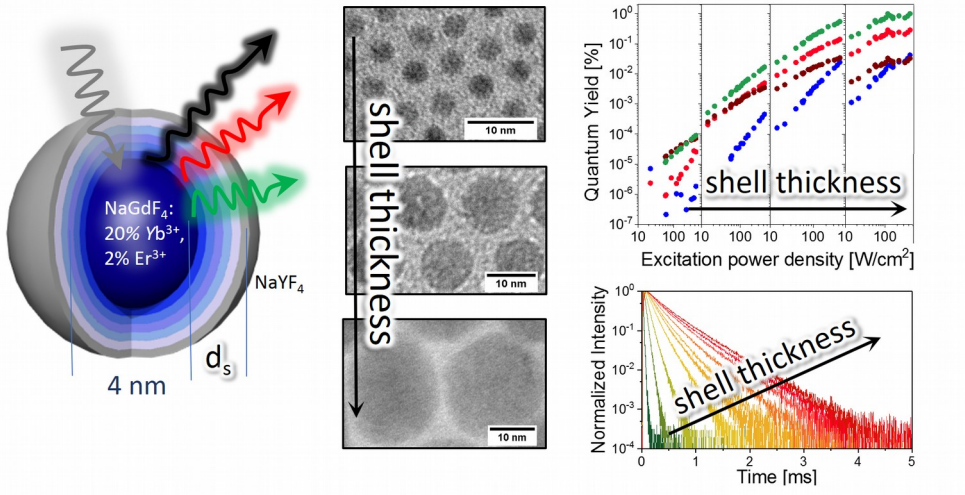
NaGdF4:
20% Yb3+,
2% Er3+
NaYF4
ds
4 nm
shell thickness
10 nm
10 nm
10 nm
Quantum Yield [%]
shell thickness
Excitation power density [W/cm2]
Normalized Intensity
shell thickness
Time [ms]